nature biotechnology

BRIEF COMMUNICATION

https://doi.org/10.1038/s41587-019-0359-9

Label-free metabolic imaging by mid-infrared optoacoustic microscopy in living cells

Miguel A. Pleitez[1,2*], Asrar Ali Khan[3,4,5,6], Alice Soldà[1,2], Andriy Chmyrov[1,2], Josefine Reber[1,2], Francesca Gasparin[1,2], Markus R. Seeger[1,2], Benedikt Schätz[1,2], Stephan Herzig[3,4,5,6], Marcel Scheideler[3,4,5,6] and Vasilis Ntziachristos[1,2*]

We develop mid-infrared optoacoustic microscopy (MiROM) for label-free, bond-selective, live-cell metabolic imaging, enabling spatiotemporal monitoring of carbohydrates, lipids and proteins in cells and tissues. Using acoustic detection of optical absorption, MiROM converts mid-infrared sensing into a positive-contrast imaging modality with negligible photodamage and high sensitivity. We use MiROM to observe changes in intrinsic carbohydrate distribution from a diffusive spatial pattern to tight co-localization with lipid droplets during adipogenesis.

Label-free dynamic imaging of biomolecules in living cells remains challenging for optical microscopy. At wavelengths below 700 nm, it is fundamentally hampered by a lack of chemical specificity or by cellular phototoxicity. Contrarily, chemically specific vibrational imaging modalities, such as spontaneous or coherent Raman scattering and mid-infrared (mid-IR) microscopy, have enormously extended possibilities for endogenous biomolecular imaging[1–3]. Stimulated Raman scattering microscopy, for instance, can rapidly image tissues at high spatial resolution[4,5]. However, Raman imaging may photodamage cells[6] and its sensitivity is above 1 mM[1], which misses biomolecules in the physiologically relevant micro- to nanomolar range. Raman imaging of carbohydrates has been demonstrated mainly in fixed cells[7,8] and in living cells after the use of labeling (that is, isotopic labeling) or glucose analogs[5,9], as well as in densely packed starch granules in microalgae[10]. Direct vibrational excitation by mid-IR absorption complements Raman imaging[3] (Supplementary Table 1). On the basis of photon absorption, rather than scattering, mid-IR spectroscopy and imaging offer cross-sections up to eight orders of magnitude larger than Raman imaging for certain molecules[3,11,12], sensitively detecting the CH bond and the fingerprint spectral region[3]. Nevertheless, this modality is poorly suited to metabolic studies of living cells because water strongly attenuates mid-IR light and because it applies negative-contrast detection (that is, the stronger the attenuation, the weaker the signal detected). Typically, samples are placed within thin cuvettes (~10–25 μm thick) and irradiated with high-powered mid-IR sources[13,14]. Such confinement perturbs normal cellular behavior and proliferation.

Here we introduce MiROM, a bond-selective imaging modality that is based on biomolecule-specific vibrational transitions and radiation-less de-excitation for highly efficient optoacoustic generation and detection (Fig. 1). We hypothesized that MiROM could offer label-free detection for all types of biomolecules with high signal-to-noise ratio (SNR) and contrast-to-noise ratio (CNR). MiROM relies on detection of ultrasound waves, which are attenuated much less than mid-IR photons; ultrasonic detection also renders MiROM as a positive-contrast method, that is, the stronger the attenuation, the stronger the signal detected. The unique combination of positive-contrast sensing and low-attenuation detection-path balances signal loss, allow deeper imaging than standard mid-IR microscopy. Here MiROM was implemented in transillumination, which allowed diffraction-limited optical excitation with confocal ultrasound detection (Fig. 1a). A mid-IR absorption–contrast micrograph was obtained by raster scanning the sample within the focal plane, simultaneously acquiring optoacoustic signal from specific biomolecular vibrations. With the system presented here, using an average laser power of only 330 μW, we obtained a limit of detection (LOD) of 2.5 mM for dimethylsulfoxide (DMSO) (Supplementary Fig. 1a,b). For comparison, coherent anti-Stokes Raman scattering (CARS) has an LOD of 70 mM for DMSO at an average laser power of ~100 mW[12,15], while stimulated Raman scattering microscopy detects up to 21 mM of DMSO at a similar irradiation power[12,16]. Moreover, we obtained an LOD of 1.5 μM for protein (albumin) in D_2O using only 500 μW laser power (Supplementary Fig. 1c–g), which promises live-cell chemical microscopy at considerably lower risk of phototoxicity[6] (Supplementary Fig. 2).

First, we demonstrated the full biomolecular-contrast coverage of MiROM in vitro in comparison with standard attenuated total reflectance Fourier-transform infrared (ATR-FTIR) spectroscopy (Fig. 1b,c, Supplementary Fig. 3 and Supplementary Tables 2–5). Next, we demonstrated its bond-selective live-cell imaging capabilities by mapping the lipid and protein content in HeLa cells, undifferentiated 3T3-L1/PreBAT preadipocytes and differentiated 3T3-L1 adipocytes. The symmetric CH_2 vibration of lipids (around 2,850 cm^{-1}) and the amide II band of proteins (around 1,550 cm^{-1}), mainly NH bending and CN stretching, were excited. Imaging wavenumbers were fine-tuned by live-cell optoacoustic spectroscopy (Fig. 1h,i). The spatial (lateral) resolution of the system (~5.3 μm at 2,850 cm^{-1}; Supplementary Fig. 4a,b) resolved single cells and individual lipid droplets (LDs) in differentiated 3T3-L1 adipocytes (Fig. 1d–h). In HeLa cells and undifferentiated preadipocytes, micrographs at the CH_2 vibration (lipid map) showed the phospholipid membrane (Supplementary Fig. 5) at CNRs up to 22:1 (SNRs around 30:1; Methods). In differentiated adipocytes, the dominant

[1]Institute of Biological and Medical Imaging, Helmholtz Zentrum München, Neuherberg, Germany. [2]Chair of Biological Imaging (CBI) and Center for Translational Cancer Research (TranslaTUM), Technische Universität München, München, Germany. [3]Institute for Diabetes and Cancer, Helmholtz Zentrum München, Neuherberg, Germany. [4]Joint Heidelberg-IDC Translational Diabetes Program, Heidelberg University Hospital, Heidelberg, Germany. [5]Molecular Metabolic Control, Medical Faculty, Technische Universität München, München, Germany. [6]German Center for Diabetes Research (DZD), Neuherberg, Germany. *e-mail: miguel.pleitez@helmholtz-muenchen.de; v.ntziachristos@helmholtz-muenchen.de

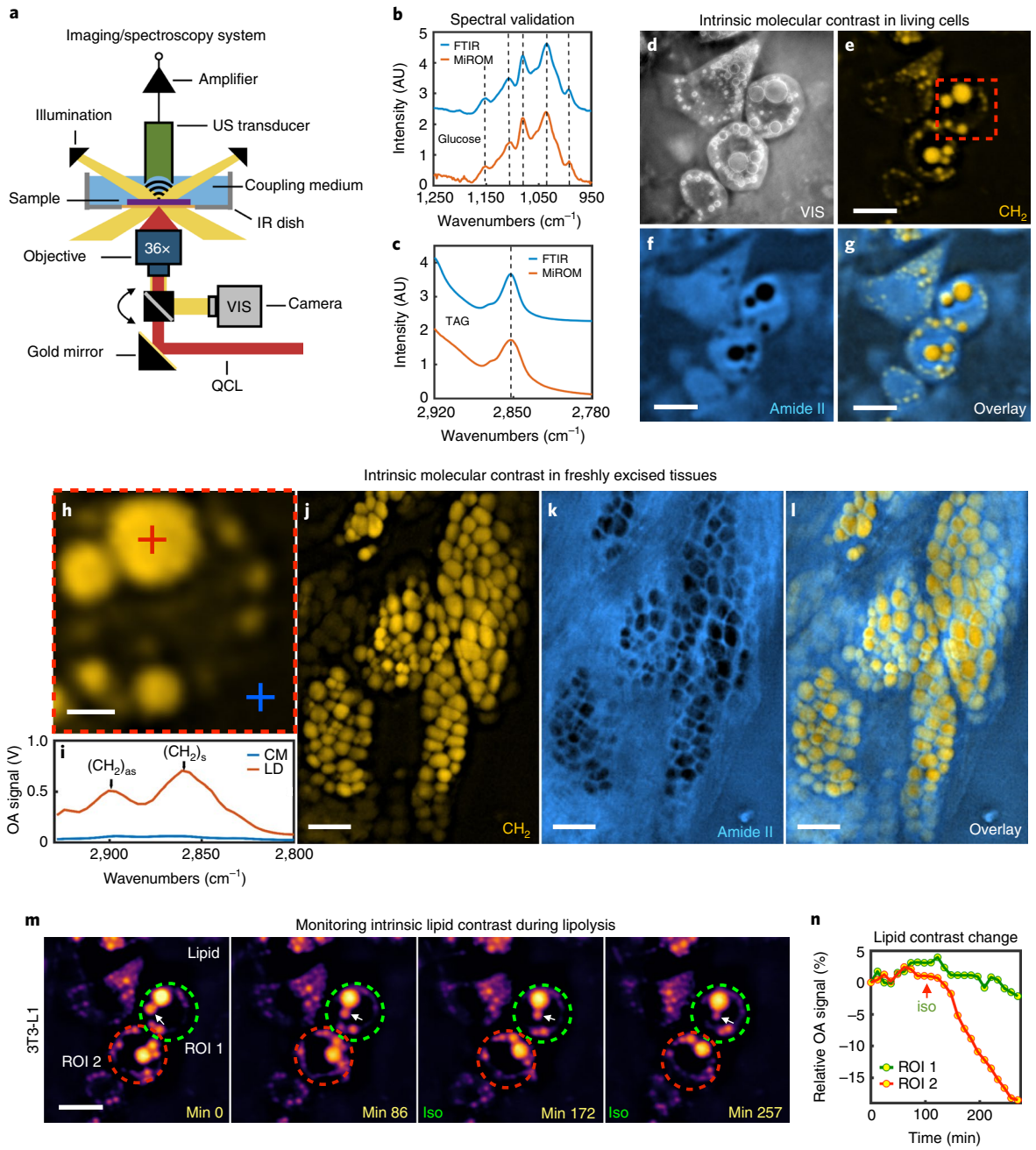

Fig. 1 | Mid-IR optoacoustic microscopy. a, Excitation-sample-sensor configuration for MiROM. Focused ultrasound (US) transducer and objective are confocally aligned to the sample plane. **b**,**c**, Comparison of MiROM and ATR-FTIR spectrum of glucose and 1,2-dioleoyl-3-palmitoyl-rac-glycerol (TAG) in vitro. The vertical dashed lines indicate good spectral matching between both methods. **d**, Brightfield visible (VIS) image of differentiated 3T3-L1 cells. **e**–**g**, MiROM micrographs of the cells (**d**) with endogenous lipid contrast (**e**) at 2,857 cm^{-1} (CH_2 vibration) and protein contrast (**f**) at 1,550 cm^{-1} (amide II). **g**, Overlay of lipid and protein maps. **h**, Expanded view of a single adipocyte, indicated by a dashed red square in **e**. Scale bar, 10 µm. Two spots for spectral analysis and fine tuning of the imaging wavelength have been marked; on a LD (red cross) and on the culture medium (CM) (blue cross). **i**, Optoacoustic (OA) spectra in the CH vibrational region for the selected spots in **h**. **j**–**l**, MiROM micrographs of freshly excised pancreatic mouse tissue of 4 mm thickness. Scale bar, 100 µm. **j**, Lipid map at 2,850 cm^{-1}. **k**, Protein map at 1,550 cm^{-1}. **l**, Overlay of lipid and protein maps. Here clusters of pancreatic acinar glands embedded in protein are observed. **m**,**n**, Monitoring induced lipolysis in differentiated 3T3-L1 adipocytes. **m**, Lipid monitoring sequence at 2,857 cm^{-1}. Two regions of interest (ROIs) enclosing individual adipocytes are marked; green dashed circle for ROI 1 and red dashed circle for ROI 2. The white arrow follows the process of LD remodeling in a single adipocyte enclosed in ROI 1. Time and presence of isoproterenol (ISO) is indicated at the bottom corners of each frame (see also Supplementary Videos 3 and 4). **n**, Relative lipid contrast change for ROI 1 and 2 in **m**; the red arrow indicates when ISO was added. **e**–**g**,**m**, Scale bars, 40 µm. Data in **b**–**n** are representative of five independent experiments.

contrast comes from LDs because they contain more triglycerides than the cell membrane and culture medium. CNRs up to 220:1 and SNRs up to 223:1 were observed.

Positive contrast in amide II micrographs (protein map) originated mainly from the overall protein content, with a weak contribution from water. CNRs up to 41:1 and SNRs around 80:1 were

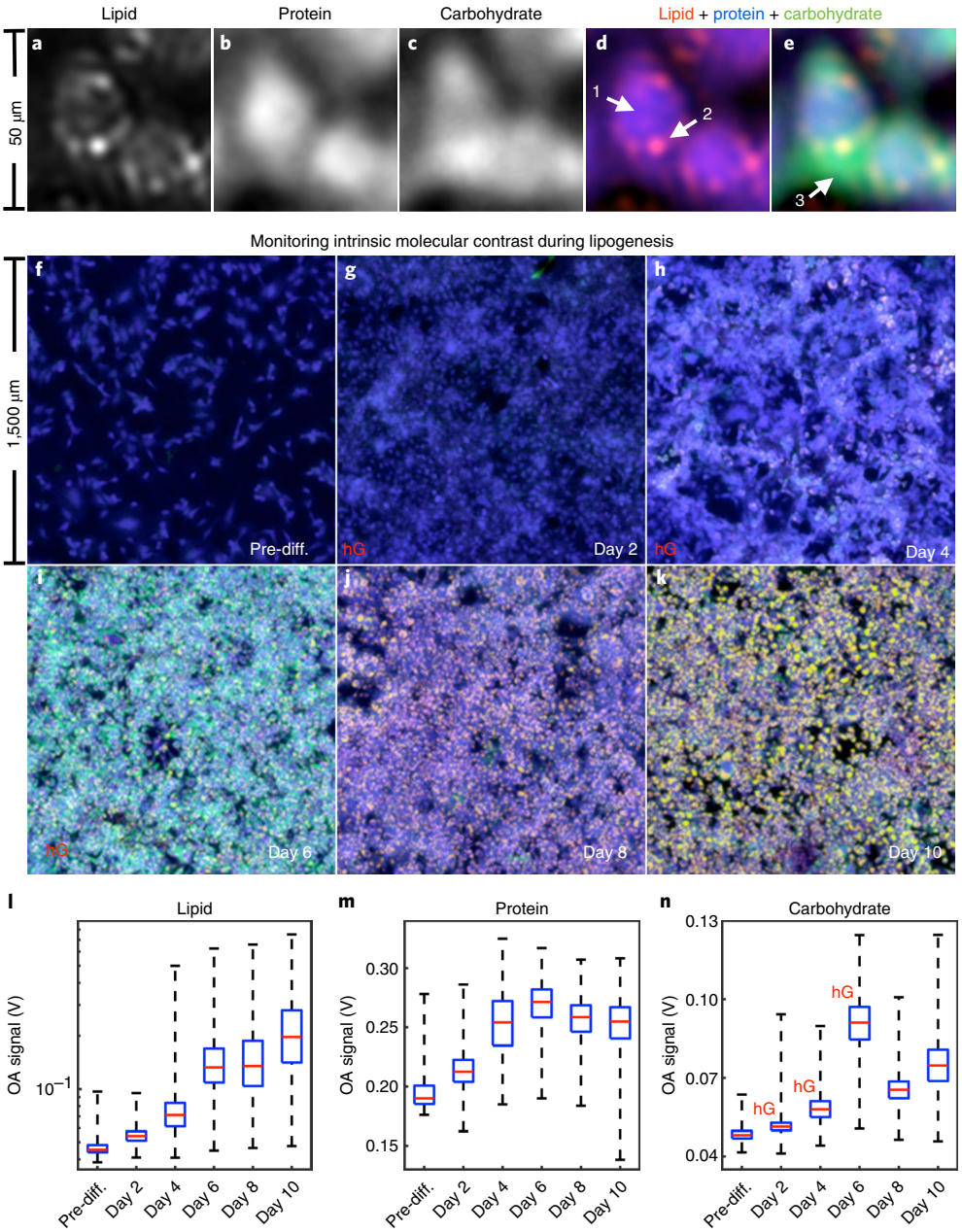

Fig. 2 | Monitoring of carbohydrate contrast on 3T3-L1 adipocytes during LD formation. a–e, MiROM micrographs of 3T3-L1 cells at differentiation day 6; imaging speed, <1 min per channel. **a**, Lipid map at 2,853 cm^{-1}. **b**, Protein map, sum of amide I and II. **c**, Carbohydrate map, sum of 1,081 cm^{-1} and 1,084 cm^{-1}. **d**, Overlay of lipid (red) and protein (blue) maps. **e**, Same picture as **d, but** adding the carbohydrate (green) map. Arrow 1 indicates proteins in the cell body, arrow 2 indicates an LD and arrow 3 indicates an area of carbohydrate accumulation around the growing LDs. **f–k**, Merged lipid (2,857 cm^{-1}), protein (1,541 cm^{-1}) and carbohydrate (1,022 cm^{-1}) maps of 3T3-L1 cells at different incubation days toward LD formation; imaging speed: 16 min per channel. The overall carbohydrate contrast increases after differentiation is started, and it is broadly distributed in the cells at day 6 (CNR of 24:1 and SNR of 40:1) around the areas of LD formation, as in **e**. At days 8 and 10, however, carbohydrate contrast is found only sparsely, but is highly co-localized with the LDs; see also Supplementary Fig. 8. **l–n**, Box plots ($n = 90{,}000$) of optoacoustic contrast for each channel in the micrographs shown in **f–k**; box plots indicate the upper and lower quartiles (box limits), median (center line) and minimum and maximum values (whiskers). During differentiation (days 2, 4 and 6), the cells show a rapid increase of molecular contrast. Once the cell medium is changed to normal incubation medium (low glucose concentration, no insulin) after day 6, lipid accumulation is observed at a lower rate while proteins reach a rather stable level and the mean carbohydrate contrast drops, correlating with extracellular glucose and insulin modulation. The label 'hG' (red) indicates when the cells were cultured with differentiation medium (high glucose concentration + insulin). Images in **a–k** are representative of five independent experiments. Pre-diff., pre-differentiation.

observed (Supplementary Fig. 6a). LDs showed negative contrast because they are hydrophobic and contain less protein than the cytoplasm. The absolute contrast of LDs in the protein map was nevertheless high enough to be detected at SNRs up to 46:1, perhaps because of LD-associated proteins (Supplementary Fig. 6a).

Besides lipids and proteins, carbohydrates were also detected in living 3T3-L1 adipocytes after excitation between 1,085 and 1,000 cm^{-1} (C–O stretching and C–O–H deformation). Localized contrast was found in the cell body around the growing LDs with CNRs up to 24:1 and SNRs around 40:1 (field of view (FOV),

50 μm × 50 μm; imaging time, <1 min per frame; Fig. 2a–e). One possible explanation for the presence of carbohydrates in the cell body might be the capture and accumulation of glucose for biosynthesis of triglycerides to be packed into LDs during lipogenesis. This observation is supported by measurements in differentiating 3T3-L1 cells where the molecular contrast (lipid, protein and carbohydrate) was monitored in large FOVs (1.5 mm × 1.5 mm) during several days (Fig. 2f–n). Glucose uptake was manipulated by changing the concentrations of glucose and insulin in the medium (Methods). Carbohydrate contrast increased in cells when incubated in 25 mM glucose and 1 μg ml^{-1} insulin (Fig. 2g–i,n; days 2, 4 and 6) and decreased when cells were incubated in 5 mM glucose only (Fig. 2j,k,n; days 8 and 10). These changes in MiROM carbohydrate contrast agreed with a standard colorimetric assay of total carbohydrate (Supplementary Fig. 7; Methods). The carbohydrate contrast was initially diffuse in the cell body and later co-localized with LDs during incubation (Supplementary Fig. 8). This may reflect the appearance of glycoproteins or glycolipids in LDs or their membranes.

We used MiROM to monitor lipid and protein dynamics during isoproterenol-induced lipolysis in white adipocytes (differentiated 3T3-L1) and brown adipocytes (differentiated PreBAT) over 4 h. Lipid (at 2,857 cm^{-1}) and protein (at 1,550 cm^{-1}) maps were taken every 5 min before and after addition of isoproterenol to the medium (Methods). In both adipocyte types, overall lipid content slowly increased before lipolysis, reflecting ongoing lipogenesis. After induction, lipid contrast decreased continuously and nearly linearly (Fig. 1m,n and Supplementary Fig. 9a–d). Different white adipocytes exhibited different lipolysis rates, with some adipocytes unaffected by isoproterenol. Absorption of smaller LDs by larger ones (that is, LD remodeling) was continuously observed in some adipocytes (Fig. 1m). Other adipocytes dimmed noticeably after lipolysis induction (Fig. 1m). The same heterogeneous response to isoproterenol was observed in brown adipocytes (Supplementary Fig. 9a,c,d). As expected, lipolysis was faster and more extensive in brown than in white adipocytes: by 2 h, lipid contrast had changed up to 30% in brown adipocytes as compared to 18% in white adipocytes (Supplementary Videos 1–4). Similar heterogeneous changes in protein contrast were observed in cells during lipolysis (Supplementary Videos 5 and 6, and Supplementary Figs. 9e,f and 10). This may reflect adipokine secretion, protein degradation and/or protein translation. Changes in protein contrast may also reflect conformational changes because amide II is relatively conformation dependent[17].

To demonstrate the potential of MiROM to image deeper in thicker samples than with standard mid-IR imaging, we applied MiROM in a 4-mm-thick slice of freshly excised pancreatic (mouse) tissue (Fig. 1j–l). Lipid micrographs show the pancreatic acinar glands in positive contrast (CNR up to 58:1), while protein micrographs show, in negative contrast, the compartments where acinar glands are embedded (CNR up to 21:1) (Supplementary Fig. 6b). Similar or higher CNRs were observed in other similarly thick tissues (Supplementary Figs. 11 and 12). A maximum imaging depth of 90 μm was obtained for the acinar glands (Supplementary Fig. 13) as compared to 575 μm in fat–polyamide-suture phantoms (Supplementary Fig. 14). Regarding imaging speed, MiROM enables imaging FOVs of 5 mm × 5 mm in steps of 10 μm (pixel size) in ~16 min.

MiROM offers unprecedentedly high contrast, image quality, sensitivity and specificity for endogenous biomolecular microscopy of living cells and thick unprocessed freshly excised tissues with negligible photodamage. For the first time, we visualize how carbohydrates initially spread through young adipocytes, then co-localize with LDs upon adipocyte maturation. MiROM can monitor intrinsic lipid and protein changes of <1% during lipolysis. MiROM is based on vibrational excitation by mid-IR absorption and positive-contrast detection, so it offers great sensitivity in the fingerprint spectral region, with LODs of 2.5 mM for DMSO and 1.5 μM for albumin at laser powers in the hundreds of microwatts. Most LDs visualized by confocal microscopy were also resolved by MiROM, though the two types of images differed slightly, especially for structures <5 μm (Supplementary Fig. 15). Resolution of mid-IR microscopy may be improved by pump-and-probe optoacoustic–optothermal signal read-out[11,18,19] or ultra-wide-bandwidth ultrasound detectors[20].

Beyond carbohydrates, lipids and proteins, MiROM can be used to analyze nucleic acids and water in practically any other cell culture or tissue (shown in vitro in Supplementary Fig. 3). In this way, MiROM supports live-cell metabolic research and analytical histology, while filling an important gap in label-free biomolecular imaging and considerably extending the contrast range of optoacoustic microscopy.

Online content

Any methods, additional references, Nature Research reporting summaries, source data, extended data, supplementary information, acknowledgements, peer review information; details of author contributions and competing interests; and statements of data and code availability are available at https://doi.org/10.1038/s41587-019-0359-9.

Received: 1 March 2018; Accepted: 12 November 2019;
Published online: 23 December 2019

References

1. Cheng, J.-X. & Xie, X. S. Vibrational spectroscopic imaging of living systems: an emerging platform for biology and medicine. *Science* **350**, aaa8870 (2015).
2. Baker, M. J. et al. Using fourier transform IR spectroscopy to analyze biological materials. *Nat. Protoc.* **9**, 1771–1791 (2014).
3. Diem, M. et al. Molecular pathology via IR and raman spectral imaging. *J. Biophotonics* **6**, 855–886 (2013).
4. Prince, R. C., Frontiera, R. R. & Potma, E. O. Stimulated raman scattering: from bulk to nano. *Chem. Rev.* **117**, 5070–5094 (2017).
5. Li, J. & Cheng, J.-X. Direct visualization of de novo lipogenesis in single living cells. *Sci. Rep.* **4**, 6807 (2014).
6. Minamikawa, T. et al. Photo-induced cell damage analysis for single- and multifocus coherent anti-stokes raman scattering microscopy. *J. Spectrosc.* **2017**, 1–8 (2017).
7. Yosef, H. K. et al. Noninvasive diagnosis of high-grade urothelial carcinoma in urine by raman spectral imaging. *Anal. Chem.* **89**, 6893–6899 (2017).
8. Kallepitis, C. et al. Quantitative volumetric raman imaging of three dimensional cell cultures. *Nat. Commun.* **8**, 14843 (2017).
9. Hu, F. et al. Vibrational imaging of glucose uptake activity in live cells and tissues by stimulated raman scattering. *Angew. Chem. Int. Ed. Eng.* **54**, 9821–9825 (2015).
10. Chiu, L., Ho, S. H., Shimada, R., Ren, N. Q. & Ozawa, T. Rapid in vivo lipid/carbohydrate quantification of single microalgal cell by Raman spectral imaging to reveal salinity-induced starch-to-lipid shift. *Biotechnol. Biofuels* **10**, 9 (2017).
11. Zhang, D. et al. Depth-resolved mid-infrared photothermal imaging of living cells and organisms with submicrometer spatial resolution. *Sci. Adv.* **2**, e1600521 (2016).
12. Zhang, C. & Cheng, J. X. Perspective: coherent raman scattering microscopy, the future is bright. *APL Photonics* **3**, 090901 (2018).
13. Haase, K., Kröger-Lui, N., Pucci, A., Schönhals, A. & Petrich, W. Real-time mid-infrared imaging of living microorganisms. *J. Biophotonics* **9**, 61–66 (2016).
14. Martin, M. C. et al. 3D spectral imaging with synchrotron fourier transform infrared spectro-microtomography. *Nat. Methods* **10**, 861–864 (2013).
15. Hong, W. et al. In situ detection of a single bacterium in complex environment by hyperspectral CARS imaging. *ChemistrySelect* **1**, 513–517 (2016).
16. Liao, C.-S. et al. Stimulated raman spectroscopic imaging by microsecond delay-line tuning. *Optica* **3**, 1377 (2016).
17. Oberg, K. A., Ruysschaert, J.-M. & Goormaghtigh, E. The optimization of protein secondary structure determination with infrared and circular dichroism spectra. *Eur. J. Biochem* **271**, 2937–2948 (2004).
18. Lee, E. S. & Lee, J. Y. High resolution cellular imaging with nonlinear optical infrared microscopy. *Opt. Express* **19**, 1378–1384 (2011).
19. Shi, J. et al. High-resolution, high-contrast mid-infrared imaging of fresh biological samples with ultraviolet-localized photoacoustic microscopy. *Nat. Photonics* **13**, 609–615 (2019).
20. Aguirre, J. et al. Precision assessment of label-free psoriasis biomarkers with ultra-broadband optoacoustic mesoscopy. *Nat. Biomed. Eng.* **1**, 0068 (2017).

Publisher's note Springer Nature remains neutral with regard to jurisdictional claims in published maps and institutional affiliations.

© The Author(s), under exclusive licence to Springer Nature America, Inc. 2019

Methods

System description. A broadly tunable pulsed quantum cascade laser (QCL) (MIRcat, Daylight Solutions) was used for optoacoustic generation and biomolecular specificity; the spectral range of the QCL was 3.4–11.0 µm (2,941–909 cm^{-1}) with a spectral linewidth of ≤1 cm^{-1} (full width at half maximum, FWHM). The pulse duration of the QCL was set to 20 ns at a repetition rate of 100 kHz then focused into the sample by a 0.5 NA reflective objective (36×, Newport Corporation). The mid-IR absorption map of the sample was obtained by scanning the sample along the focal plane by motorized stages (Prior Scientific and Physik Instrumente) simultaneously detecting the optoacoustic signal by a 20 or 25 MHz central frequency focused ultrasound transducer (Imasonic and Sonaxis). The focused ultrasound transducer and the reflective objective were coaxially aligned to share the same focal plane where the sample was placed on a custom-made mid-IR transparent stainless-steel or acrylic–glass dish using a ZnSe window (Edmund Optics) or a ZnS window (Crystal) as bottom substrate. For the live-cell studies, the cell medium served as acoustic coupling between the ultrasound transducer and the cells. Deionized water was used as the coupling medium otherwise.

To remove interference from atmospheric CO_2 and water vapor, the mid-IR beam-path was purged with a constant flow of dry N_2. A mercury–cadmium–tellurium (MCT) detector (Daylight Solutions) was used for optical reference and a VIS laser pointer, co-aligned with the QCL beam, served as aiming beam for easy optical adjustment. For validation, co-registration and easy ROI selection, oblique VIS illumination (Edmund Optics) was used to obtain standard brightfield micrographs with a general purpose monochromatic camera (Edmund Optics) (Fig. 1a and Supplementary Fig. 4a).

The laser power at selected and relevant wavenumbers for this work was measured by a mid-IR specific power meter (PE9-ES-C, Ophir-Spiricon) at a 500 ns laser pulse duration and 10 kHz repetition rate just before entering the reflective objective. The average laser power at the sample was calculated scaling the measured values to the pulse duration of 20 ns and repetition rate of 100 kHz, also taking into account the obscuration (17%) of the reflective objective. These laser excitation powers were used for all measurements reported here including: imaging, spectroscopy and viability test. This is summarized in the table below.

Wavenumber (cm^{-1})	Measured average power at 500 ns and 10 kHz (mW)	Equivalent laser power at 20 ns, 100 kHz and 17% obscuration (mW)
2,850	0.8	0.27
1,650	1.6	0.53
1,550	2.0	0.66
1,085	1.9	0.33

Signal recovery, contrast and noise. The raw optoacoustic signals were amplified by 63 dB (MITEQ) filtered with a 50-MHz low pass filter (Mini-Circuits) and then recorded at a sampling rate of 250 MS s^{-1} on a 12-bit DAQ card, or at 200 MS s^{-1} on a 16 DAQ card, (Gage Applied). The intensity of each pixel composing the micrographs shown in this work was the peak-to-peak amplitude value resulting from the average of 50 or 100 optoacoustic transients (A-lines); corresponding to a pixel dwell time of 1 ms or 500 µs, respectively, at a pulse repetition rate of 100 kHz.

The SNR is defined here as the ratio between the peak-to-peak amplitude value of the optoacoustic signal (OAS_{PkPk}) over the peak-to-peak amplitude value of the noise level ($Noise_{PkPk}$) before the arrival of the optoacoustic signal. For instance, the maximum SNR of the lipid map for the white adipocytes discussed above is 223:1, corresponding to a relative error of 0.45%. In terms of absolute values, this corresponds to an OAS_{PkPk} of 702.2 mV and a $Noise_{PkPk}$ of 3.1 mV. In the protein map the maximum SNR is close to 80:1, or 1.3% relative error. This is calculated from an absolute OAS_{PkPk} amplitude of 247 mV and a noise level of around 3 mV.

$$\mathrm{SNR} = \mathrm{OAS_{PkPk}}/\mathrm{Noise_{PkPk}}$$

The CNR is defined here as the intensity difference between a point in the sample (OA_S) and a point in the background (OA_B) divided over $Noise_{PkPk}$.

$$\mathrm{CNR} = |\mathrm{OA_S} - \mathrm{OA_B}|/\mathrm{Noise_{PkPk}}$$

The mean contrast-to-background ratio described in Supplementary Fig. 7 is the mean contrast obtained from the image histogram divided over the background intensity (OA_B).

As explained below, before measurements on cells and tissues, the contrast, resolution, spectral accuracy, sensitivity and imaging depth of the system were tested in synthetic samples: polyamide sutures and polyethylene microspheres embedded in agar, NIST spectral gold standard and DMSO (Supplementary Figs. 1 and 4b–d, Fig. 14, and Supplementary Table 6).

Spectral validation. First, the absorption spectrum of an NIST traceable polystyrene calibration film for IR spectroscopy (Sigma-Aldrich) was measured in transmission mode by MiROM. The position of the absorption peaks obtained by MiROM was compared with the certified values of the NIST gold standard. We obtained a minimum deviation of 0.1 cm^{-1} around 1,583 cm^{-1} and a maximum deviation of 2.6 cm^{-1} around 2,850 cm^{-1} of the spectrum measured by MiROM regarding the gold standard (Supplementary Table 6).

Second, the ability to identify specifically and precisely different biomolecules was demonstrated by comparing the optoacoustic spectra obtained by MiROM with the spectra of the same molecules (the same samples) obtained with a standard ATR-FTIR spectrometer (Bruker Corporation).

Four samples representing each of the fundamental classes of biomolecules (namely glucose, DNA, triglycerides and albumin) were prepared and measured with MiROM and ATR-FTIR as follows. A 50 g l^{-1} water solution of glucose was prepared by dissolving 2.5 g of D-(+)-glucose (Sigma-Aldrich) in 50 ml of distilled water. A 5% water solution of DNA (deoxyribonucleic acid sodium salt from *Escherichia coli* strain B, Sigma-Aldrich) was prepared by dissolving 1 mg of DNA in 20 µl of distilled water. A 5-µl drop of this solution was placed in a carbon tape ring located on a dish and dried under vacuum. The sample was covered with a plastic film to avoid water dilution.

A 10 mg ml^{-1} solution of 1,2-dioleoyl-3-palmitoyl-rac-glycerol (Sigma-Aldrich) was prepared by dissolving 1 mg in 100 µl of a chloroform–methanol solution (2:1). A 10-µl drop of this solution was placed on the window of a dish and dried under vacuum.

An 80 g l^{-1} D_2O solution of albumin was prepared by dissolving 2.0 g of albumin (Carl Roth) in 25 ml of heavy water. As commonly done in standard FTIR spectroscopy, for albumin, D_2O was used instead of H_2O to avoid the strong absorption peak of water around 1,650 cm^{-1} (Supplementary Fig. 3d), which overlaps the amide I band of proteins.

All the measurements were performed on the custom-made mid-IR dish with a ZnSe window using carbon tape (SPI Suppliers) as spectral reference. The optoacoustic spectra were measured with a resolution of 2 cm^{-1} and an averaging time of 100 ms per wavenumber. For comparison, a 5-µl drop of each solution was measured with the ATR-FTIR spectrometer equipped with a diamond ATR crystal. The same resolution of 2 cm^{-1}, as with the MiROM system, was used to record the spectra with the ATR-FTIR spectrometer. For water solutions, water was measured and subtracted from both, the optoacoustic and FTIR spectra. As observed in Fig. 1b,c, Supplementary Fig. 3 and Supplementary Tables 2–5, MiROM was able to accurately detect the absorption bands of biomolecules.

Determination of the limit of detection. We determined the LOD of MiROM for two reference molecules: DMSO in H_2O and albumin in D_2O. For DMSO, the optoacoustic spectrum at different concentrations (from 664 mM to 0.02 mM) was measured between 1,250 and 909 cm^{-1}, averaging time ~100 ms per wavenumber (Supplementary Fig. 1a). The area under the absorption band of the S=O vibration at 1,010 cm^{-1} was selected for determination of the lowest detectable concentration of DMSO, the optoacoustic signals at 1,066 cm^{-1} and 984 cm^{-1} were used for spectral baseline correction and normalization, respectively. The area under the normalized optoacoustic intensity of the S=O vibration (Supplementary Fig. 1b), as well as its optoacoustic spectra, showed that DMSO could be detected, above the spectral baseline, at a concentration of 2.5 mM with a SNR of 6:1. Here, the baseline, or noise level, is defined by the difference of two measured optoacoustic spectra of water. The maximum average laser power in the spectral range measured is 330 µW at around 1,085 cm^{-1}, measured as described above.

For albumin, the optoacoustic spectrum at different concentrations (from 750 µM to 1.5 µM) was measured between 1,700 and 1,600 cm^{-1} (the amide I band), averaging time ~100 ms per wavenumber (Supplementary Fig. 1d). The area under the amide I band was selected for determination of the lowest detectable concentration of albumin, the optoacoustic signal at 1,700 cm^{-1} and 1,600 cm^{-1} were used for spectral baseline correction and normalization, respectively. The area under the normalized optoacoustic intensity of the amide I band (Supplementary Fig. 1e), as well as its optoacoustic spectra, showed that albumin could be detected, above the spectral baseline, at a concentration of 1.5 µM with an SNR of 4.5:1. Here, the baseline, or noise level, is defined by the difference of two measured optoacoustic spectra of heavy water. The maximum average laser power in the spectral range measured is 530 µW at around 1,650 cm^{-1}, measured as described above.

The SNR for the LOD determination (SNR_{LOD}) is defined here as the area of the normalized optoacoustic absorption band of the analyte ($Area_{NOAS}$; the signal), after buffer subtraction, divided by the area of the baseline ($Area_{BL}$; the noise) (absolute value).

$$\mathrm{SNR_{LOD}} = \mathrm{Area_{NOAS}}/\mathrm{Area_{BL}}$$

Image processing. To enhance visibility and compensate for spatial resolution of mid-IR microscopy in the range of the subcellular compartments of interest (~5 µm), the images were bicubic interpolated to a pixel size of 250 nm and deconvolved with the experimentally determined point-spread function (Supplementary Fig. 4b) by a three- or five-step iterative Wiener deconvolution. Furthermore, the images were post processed by a 2-pixel Gaussian filtering, outlier removal if necessary, a contrast enhancement to a 0.3% saturation and a histogram normalization. For resolution analysis and SNR determination, the

images were kept unprocessed. For co-localization analysis, we applied non-masked and non-thresholded Pearson correlation coefficients (ImageJ, v1.52i; coloc2 plugin) to the unprocessed images.

Preparation and measurement of white and brown adipocytes. 3T3-L1 mouse white preadipocyte cells were plated in custom plates and cultured till confluency in growth medium consisting of: low-glucose (1 g l^{-1}) DMEM (Life Technologies) supplemented with 10% FBS (Merck) and 1% penicillin–streptomycin (Life Technologies). Cells were kept in an incubator at 37 °C, 5% CO_2. The process of differentiation lasted for 6 d. On day 0 and day 2, differentiation medium (high-glucose (4.5 g l^{-1}) DMEM, 10% FBS, 1% penicillin–streptomycin, 1 µg ml^{-1} insulin (Sigma-Aldrich), 0.25 µM dexamethaxone (Sigma-Aldrich), 0.5 mM 3-isobutyl-1-methylxanthine (Sigma-Aldrich) and 1/1,000 volume ABP (50 mg ml^{-1} L-ascorbate, 1 mM biotin, 17 mM pantothenate (Sigma))) was added to the cells. On day 4, differentiation medium supplemented only with insulin and ABP was used. From day 6 and on (after MiROM measurements) the cells were kept in growth medium (low glucose, no insulin).

The PreBAT cell line was created and provided by J. Hoppmann, et al. (Department of Internal Medicine I, University of Luebeck, Germany) by immortalizing preadipocytes from the intrascapular BAT of newborn mice using the SV40 Large T antigen. The differentiation process also lasted for 6 d starting with induction on day 0 with DMEM growth medium (4.5 g l^{-1} glucose; Life Technologies) containing 20% FBS (Merck) and 1% penicillin–streptomycin (Life Technologies) with the addition of 20 nM insulin (Sigma-Aldrich), 1 µM triiodothyronine (Sigma-Aldrich), 0.125 mM indomethacin (Sigma-Aldrich), 2 µg ml^{-1} dexamethasone (Sigma-Aldrich) and 0.5 mM 3-isobutyl-1-methylxanthine (Sigma-Aldrich). The cells were kept in the incubator at 37 °C, 5% CO_2. On day 2 and day 4, growth medium containing only insulin and triiodothyronine was added and on day 6 the cells were given only growth medium. At the end of differentiation, both cell lines showed abundant amounts of lipid droplets.

All MiROM measurements on cells were performed using growth medium; changing from differentiation medium to growth medium right before imaging whenever needed.

Quantification of total carbohydrates content. The total amount of carbohydrates in the differentiated 3T3-L1 cell lysates were measured using the Cell Biolabs Total Carbohydrate Assay kit (STA-682, Cell Biolabs) following the manufacturer's protocol. After each MiROM measurement (at day 0, 2, 4, 6, 8 and 10), the cells were removed from the customized plates upon trypsin digestion and centrifuged at 2,000 rpm for 3 min. The supernatant was discarded and the pellet was washed once with PBS. After centrifugation, the cells were collected and stored at −80 °C. The cells were resuspended at $1–2 \times 10^6$ cells ml^{-1} in 1× assay buffer. Each pellet was vigorously homogenized and centrifuged to remove the debris. Cell lysates were assayed undiluted in a 96-well plate, 30 µl of each solution was mixed with 150 µl of concentrated sulfuric acid and incubated for 15 min at 90 °C. After addition of a developing solution, containing 5% phenol in 1× diluent buffer, a chromogen is formed and it can be detected at 490 nm. The samples were analyzed with the microplate reader CLARIOstar (BMG LABTECH) at an optical density of 490 nm. For each point, the background optical density (acquired before the addition of the developing solution) was subtracted. Experiments were carried out in duplicate.

Cell-viability study. To assess the negligibility of photodamage induced by MiROM, a standard viability test on undifferentiated 3T3-L1 preadipocytes was performed. A 10-µl drop of cells was plated in a custom-made MiROM dish, with a ZnSe window 12.7 mm in diameter. After overnight incubation in growth medium, at 37 °C, 5% of CO_2, a FOV of 2 mm × 2 mm was irradiated with a pulse laser of 100 kHz during a total irradiation time of 280 min: 20 scanning loops (frames) for each excitation wavenumber (1,557 and 2,850 cm^{-1}), corresponding to 7 min per frame. During the measurement, the cells were kept at 37 °C. Cell viability was assessed using erythrosine B exclusion assay. Cell survival was expressed as the percentage ratio of viable irradiated cells as compared to the corresponding viable non-irradiated controls. For statistical elaboration OriginPro9.1 Software was used. Reported data corresponded to the mean ± s.d. from three experiments.

Preparation and measurement of mouse tissues. Male C57BL/6J mice (8–10 weeks old; Charles River Laboratories) were kept at 24 ± 1 °C and fed with standard rodent diet (Altromin 1314, Altromin Spezialfutter) with free access to water, constant humidity and a 12-h light–dark cycle. After the mice were killed, organs were collected and directly placed on the sample holder where they were covered with low-melting-temperature agar (2%) and deionized water as coupling medium.

Reporting Summary. Further information on research design is available in the Nature Research Reporting Summary linked to this article.

Data availability

The data that support the findings of this study are available from the corresponding authors upon reasonable request.

Acknowledgements

The research leading to these results has received funding from the Deutsche Forschungsgemeinschaft (DFG), Germany (Gottfried Wilhelm Leibniz Prize 2013; NT 3/10-1), as well as from the European Research Council (ERC) under the European Union's Horizon 2020 research and innovation program under grant agreement No 694968 (PREMSOT). The authors thank A. Georgiadi for advice, discussion and support on mouse adipocyte tissue preparation.

Author contributions

M.A.P. created the imaging concept, designed, built and characterized the imaging system. M.A.P., A.A.K. and J.R. designed and performed the experiments on adipocytes. M.A.P. and J.R. designed and performed the experiments on excised tissues. A.C. synchronized and automated the imaging system. M.R.S. performed the image processing and prepared the art work. M.A.P. and A.S. designed and performed the molecular contrast validation experiments and viability tests on cells. M.A.P., F.G. and B.S. designed and performed the spectral validation of the system. M.A.P. processed the results, prepared the images, and wrote the manuscript. M.A.P., A.A., J.R. and M.S. analyzed the results on lipolysis. M.S. and S.H. supervised the study on lipolysis. V.N. supervised the whole study. All authors edited the manuscript.

Competing interests

V.N. has financial interests in iThera Medical (equity owner and consultant); SurgVision B /Bracco Sp.A (member of the scientific advisory board); and Spear UG (owner). These companies, however, did not contribute to this work. V.N. and M.A.P. are inventors on a provisional patent application related to mid-infrared optoacoustic microscopy.

Additional information

Supplementary information is available for this paper at https://doi.org/10.1038/s41587-019-0359-9.

Correspondence and requests for materials should be addressed to M.A.P. or V.N.

Reprints and permissions information is available at www.nature.com/reprints.

nature research

Corresponding author(s): Vasilis Ntziachristos, Miguel A. Pleitez

Last updated by author(s): Nov 5, 2019

Reporting Summary

Nature Research wishes to improve the reproducibility of the work that we publish. This form provides structure for consistency and transparency in reporting. For further information on Nature Research policies, see Authors & Referees and the Editorial Policy Checklist.

Statistics

For all statistical analyses, confirm that the following items are present in the figure legend, table legend, main text, or Methods section.

n/a	Confirmed	
☐	☒	The exact sample size (*n*) for each experimental group/condition, given as a discrete number and unit of measurement
☐	☒	A statement on whether measurements were taken from distinct samples or whether the same sample was measured repeatedly
☐	☒	The statistical test(s) used AND whether they are one- or two-sided *Only common tests should be described solely by name; describe more complex techniques in the Methods section.*
☒	☐	A description of all covariates tested
☒	☐	A description of any assumptions or corrections, such as tests of normality and adjustment for multiple comparisons
☐	☒	A full description of the statistical parameters including central tendency (e.g. means) or other basic estimates (e.g. regression coefficient) AND variation (e.g. standard deviation) or associated estimates of uncertainty (e.g. confidence intervals)
☐	☒	For null hypothesis testing, the test statistic (e.g. *F*, *t*, *r*) with confidence intervals, effect sizes, degrees of freedom and *P* value noted *Give P values as exact values whenever suitable.*
☒	☐	For Bayesian analysis, information on the choice of priors and Markov chain Monte Carlo settings
☒	☐	For hierarchical and complex designs, identification of the appropriate level for tests and full reporting of outcomes
☒	☐	Estimates of effect sizes (e.g. Cohen's *d*, Pearson's *r*), indicating how they were calculated

Our web collection on statistics for biologists contains articles on many of the points above.

Software and code

Policy information about availability of computer code

Data collection	MatLab_R2016a
Data analysis	MatLab_R2016a, ImageJ 2.0.0-rc-64, OriginPro9.1

For manuscripts utilizing custom algorithms or software that are central to the research but not yet described in published literature, software must be made available to editors/reviewers. We strongly encourage code deposition in a community repository (e.g. GitHub). See the Nature Research guidelines for submitting code & software for further information.

Data

Policy information about availability of data

All manuscripts must include a data availability statement. This statement should provide the following information, where applicable:

- Accession codes, unique identifiers, or web links for publicly available datasets
- A list of figures that have associated raw data
- A description of any restrictions on data availability

The data that support the findings of this study are available from the corresponding authors upon reasonable request.

Field-specific reporting

Please select the one below that is the best fit for your research. If you are not sure, read the appropriate sections before making your selection.

☒ Life sciences ☐ Behavioural & social sciences ☐ Ecological, evolutionary & environmental sciences

Life sciences study design

All studies must disclose on these points even when the disclosure is negative.

Sample size	No sample-size calculation was performed. Sample size was defined by sample availability; pixel-size, in case of the micrograph analysis, or a minimum of three measured samples per experiment whenever possible.
Data exclusions	No data was excluded from the analysis of the optoacoustic signals, imaging formation, and/or contrast monitoring. For the 3T3-L1 cell in figure 1, however, additional micrographs at 1085 cm-1 were measured and decided not to show since the aim of this figure is to present the ability to monitor lipids, no exclusion criteria was pre-established. These additional frames at the mentioned wavelength are available upon request.
Replication	All experiments presented here been successfully repeated several times with similar results, the number of repeated experiments is indicated in the figure legends.
Randomization	The experiments were not randomized.
Blinding	The investigators were not blinded to allocation during experiments and outcome assessment.

Reporting for specific materials, systems and methods

We require information from authors about some types of materials, experimental systems and methods used in many studies. Here, indicate whether each material, system or method listed is relevant to your study. If you are not sure if a list item applies to your research, read the appropriate section before selecting a response.

Materials & experimental systems

n/a	Involved in the study
☒	☐ Antibodies
☐	☒ Eukaryotic cell lines
☒	☐ Palaeontology
☐	☒ Animals and other organisms
☒	☐ Human research participants
☒	☐ Clinical data

Methods

n/a	Involved in the study
☒	☐ ChIP-seq
☒	☐ Flow cytometry
☒	☐ MRI-based neuroimaging

Eukaryotic cell lines

Policy information about cell lines

Cell line source(s)	The 3T3-L1 mouse white preadipocytes were ordered from ATCC (www.lgcstandards-atcc.org). The PreBAT cell line was created and provided by Hoppmann, Perwitz et al. (2010), HeLa (Epithelial, Human, Cervix, Adenocarcinoma) cell lines were purchased from ATCC (www.lgcstandards-atcc.org).
Authentication	None of the cell lines used were authenticated
Mycoplasma contamination	All cultured cells were tested negative for mycoplasma contamination by PCR.
Commonly misidentified lines (See ICLAC register)	No commonly misidentified lines were used in this study.

Animals and other organisms

Policy information about studies involving animals; ARRIVE guidelines recommended for reporting animal research

Laboratory animals	Male C57BL/6J mice, 8-10 weeks old. (Charles River Laboratories Inc, Charleston, USA)
Wild animals	This study did not involve wild animals
Field-collected samples	This study did not involve field-collected samples
Ethics oversight	No ethical approval or guidance was required because the measurements were performed ex vivo

Note that full information on the approval of the study protocol must also be provided in the manuscript.